

Adsorption behavior of triphenylene on Ru(0001) investigated by scanning tunneling microscopy

Li-Wei Jing(井立威), Jun-Jie Song(宋俊杰), Yu-Xi Zhang(张羽溪), Qiao-Yue Chen(陈乔悦), Kai-Kai Huang(黄凯凯), Han-Jie Zhang(张寒洁), Pi-Mo He(何丕模)

Citation: Chin. Phys. B, 2019, 28 (**7**): 076801. DOI: 10.1088/1674-1056/28/7/076801
http://cpb.iphy.ac.cn; http://iopscience.iop.org/cpb

What follows is a list of articles you may be interested in

Superconducting state in $Ba_{(1-x)}Sr_xNi_2As_2$ near the quantum critical point

Chengfeng Yu(余承峰), Zongyuan Zhang(张宗源), Linxing Song(宋林兴), Yanwei Wu(吴彦玮), Xiaoqiu Yuan(袁小秋), Jie Hou(侯杰), Yubing Tu(涂玉兵), Xingyuan Hou(侯兴元), Shiliang Li(李世亮), and Lei Shan(单磊)

Chin. Phys. B, 2024, 33 (**6**): 066802. DOI: 10.1088/1674-1056/ad334a

Reconstruction and stability of Fe_3O_4(001) surface: An investigation based on particle swarm optimization and machine learning

Hongsheng Liu(柳洪盛), Yuanyuan Zhao(赵圆圆), Shi Qiu(邱实), Jijun Zhao(赵纪军), and Junfeng Gao(高峻峰)

Chin. Phys. B, 2023, 32 (**5**): 056802. DOI: 10.1088/1674-1056/acb9e4

Thermo-controllable self-assembled structures of single-layer 4, 4"-diamino-p-terphenyl molecules on Au (110)

Junhai Ren(任俊海), Deliang Bao(包德亮), Li Dong(董立), Lei Gao(高蕾), Rongting Wu(武荣庭), Linghao Yan(闫凌昊), Aiwei Wang(王爱伟), Jiahao Yan(严佳浩), Yeliang Wang(王业亮), Shixuan Du(杜世萱), Qing Huan(郇庆), Hongjun Gao(高鸿钧)

Chin. Phys. B, 2017, 26 (**8**): 086801. DOI: 10.1088/1674-1056/26/8/086801

Thick c-BN films deposited by radio frequency magnetron sputtering in argon/nitrogen gas mixture with additional hydrogen gas

Yan Zhao(赵艳), Wei Gao(高伟), Bo Xu(徐博), Ying-Ai Li(李英爱), Hong-Dong Li(李红东), Guang-Rui Gu(顾广瑞), Hong Yin(殷红)

Chin. Phys. B, 2016, 25 (**10**): 106801. DOI: 10.1088/1674-1056/25/10/106801

Preparation and characterization of thick cubic boron nitride films

Wang Ming-E (王明娥), Ma Guo-Jia (马国佳), Dong Chuang (董闯), Gong Shui-Li (巩水利)

Chin. Phys. B, 2014, 23 (**6**): 066805. DOI: 10.1088/1674-1056/23/6/066805

RAPID COMMUNICATION

Cascade of low-energy surface phonon modes on the B-terminated EuB_6 surface

Yumeng Li(李雨萌)[1,2,†], Meng Li(李萌)[1,2,†], Lijing Huang(黄丽静)[1,2,†], Haitao Yang(杨海涛)[1,2,3], Hongqin Xiao(肖洪钦)[1,2], Yuxuan He(何昱萱)[1,2], Geng Li(李更)[1,2,3,‡], and Hong-Jun Gao(高鸿钧)[1,2,3]

[1] *Beijing National Center for Condensed Matter Physics and Institute of Physics, Chinese Academy of Sciences, Beijing* 100190, *China*
[2] *School of Physical Sciences, University of Chinese Academy of Sciences, Beijing* 100190, *China*
[3] *Hefei National Laboratory, Hefei* 230088, *China*

(Received 26 March 2026; revised manuscript received 17 April 2026; accepted manuscript online 28 April 2026)

EuB_6 has emerged as a leading candidate magnetic Weyl semimetal, in which spontaneous ferromagnetic order breaks time-reversal symmetry and drives a topological phase transition accompanied by band inversion. Optical studies have extensively investigated the phonon modes associated with the B_6 octahedra, whose internal vibrations play an important role in understanding the physical properties of EuB_6. However, the low-energy phonon modes and their coupling to electrons remain largely unexplored. Here we report a cascade of low-energy phonon modes resolved on the B-terminated surface of EuB_6 prepared by low-temperature *in situ* cleavage. We show that defects significantly modulate the local electron–phonon coupling (EPC) strength. Moreover, a defect-pinned $\sqrt{2}\times\sqrt{2}$ short-range order emerges on the B-terminated surface, which selectively modulates the local density of states (LDOS) and the EPC strength. Our results provide insight into the interplay between low-energy surface phonons, defects, and electron–phonon coupling on the B-terminated surface of EuB_6.

Keywords: EuB_6, inelastic electron tunneling spectroscopy, surface phonons, electron–phonon coupling, short-range order

PACS: 68.35.B–, 68.35.Ja, 63.20.kd, 68.37.Ef, 64.60.Cn

DOI: 10.1088/1674-1056/ae6568 **CSTR:** 32038.14.CPB.ae6568

In low-carrier systems with localized magnetic moments, the energy scales of spin excitations and lattice vibrations are often comparable and can strongly influence charge dynamics.[1–5] Such interplay has been invoked to explain emergent phenomena including magnetic polaron formation.[6–9] A representative materials family is RB_6 (R = Sm, Eu, Yb and Ce), which hosts diverse electronic ground states ranging from mixed-valence Kondo insulators to low-carrier ferromagnets.[10–12] Their (001) surfaces are strongly polar and exhibit a charge discontinuity,[13,14] often resulting in coexisting rare-earth-terminated and B-terminated domains together with surface charge compensation.[14–16] This complexity makes it challenging to directly relate a given surface structure to its low-energy spectral response. Within this family, optical probes such as Raman and infrared spectroscopy have been widely used to assign the symmetry and energy of Γ-point optical phonons.[17,18] In several RB_6 compounds, spectral anomalies associated with magnetic order or magnetic scattering channels have been reported, suggesting coupling among spin, lattice, and charge degrees of freedom.[7,8,17,19,20] However, these optical probes are constrained by the long-wavelength limit and selection rules; full phonon-branch coverage and local-environment-dependent coupling variations are therefore often inaccessible.[21,22]

As a prototypical low-carrier ferromagnet in the RB_6 family, EuB_6 has been extensively studied by transport and optical probes.[8,9,17,23–29] Near the Curie temperature, a macroscopic picture has emerged involving ferromagnetic order,[17,26,30] colossal magnetoresistance,[9,31] and magnetic-polaron-related[6–8] behavior. These studies suggest that the coupling between lattice and spin degrees of freedom near the critical point can influence low-energy electrons.[31] Consistently, Raman and infrared spectroscopy on EuB_6 have identified several Γ-point optical phonon modes and their symmetry indicators, and modifications of optical line shapes associated with magnetic correlations have also been reported.[7,17] Nevertheless, experimental evidence for lower-energy vibrational channels, particularly those away from the Γ point or sensitive to local environments, remains limited. By contrast, inelastic electron tunneling spectroscopy (IETS) can resolve features associated with local electron-vibration coupling.[5] It can provide complementary clues for low-energy vibrations that are invisible in, or difficult to separate by, optical spectra.

In this work, scanning tunneling microscopy/spectroscopy

[†] These authors contributed equally to this work.

[‡] Corresponding author. E-mail: gengli.iop@iphy.ac.cn

© 2026 Chinese Physical Society and IOP Publishing Ltd. All rights, including for text and data mining, AI training, and similar technologies, are reserved.

(STM/S) and IETS are performed on the B-terminated surface of EuB_6 after *in situ* cleavage at low temperature. On the B-terminated surface, a cascade of inelastic channels is resolved at approximately 11 mV, 31 mV, 55 mV, and 93 mV. While the $\sim$ 93 meV feature matches the energy scale of the T_{2g} shear Raman mode of the B_6 octahedra,[7,32] the remaining low-energy modes cannot be straightforwardly assigned to previously reported Raman-active phonons, suggesting additional surface phonon modes. Near defects, the low-energy electronic states around the Fermi level are markedly enhanced, whereas the energies of these inelastic channels remain nearly unchanged and their excitation probabilities are redistributed in a mode-selective manner. This behavior indicates that defects modulate the local electron–phonon coupling strength without shifting the mode energies. Furthermore, Fourier analysis reveals a $\sqrt{2}\times\sqrt{2}R45^\circ$ short-range order with a finite correlation length near defects, suggesting that the B-terminated surface may achieve local charge compensation and structural reorganization through defect pinning.

EuB_6 crystallizes in the CaB_6-type simple-cubic structure (space group $Pm\bar{3}m$; Fig. 1(a)). B atoms form B_6^{2-} octahedra connected by inter-octahedral B–B bonds, while Eu^{2+} ions donate electrons to the boron framework, giving the material a mixed ionic-covalent character. The (001) surface is strongly polar because oppositely charged layers stack alternately along the surface normal.[33,34] Consequently, cleavage often produces surfaces with different terminations and varying degrees of surface reconstruction.

Single crystals of EuB_6 were grown using the Al-flux method.[25] Starting materials with a molar ratio of Eu:B:Al = 1:8:100 were loaded into an alumina crucible and heated to 1773 K under high-purity Ar. Then, the furnace was slowly cooled to 1573 K at 2 K/h before cooling to room temperature. The obtained crystals were washed with an NaOH solution and deionized water, yielding black cubic crystals. STM measurements were performed in a home-built system with a base pressure below 1×10^{-10} mbar at a temperature of 4.2 K.[35] Electrochemically etched tungsten tips were used in constant-current mode with the bias voltage applied to the sample. STS and IETS were acquired using a lock-in technique with a modulation amplitude of 10 mV at 971 Hz.

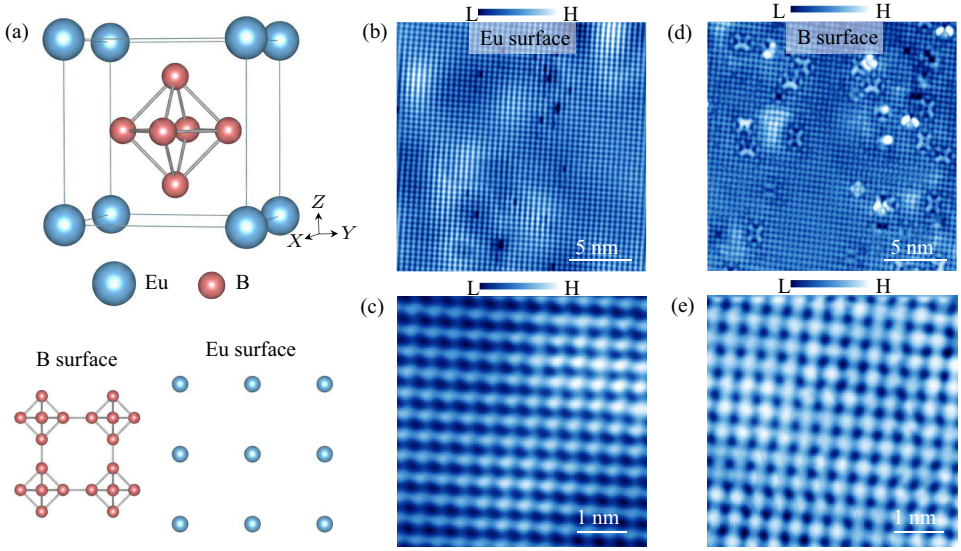


Fig. 1. Crystal structure of EuB_6 and STM images of the two terminating surfaces. (a) Schematic of the CaB_6-type simple cubic structure of EuB_6, consisting of a simple cubic Eu sublattice and a network of B_6 octahedra at the body-center positions. (b) STM image ($V_s = -200$ mV, $I_t = 200$ pA) of the Eu-terminated surface. (c) Zoom-in STM image ($V_s = -200$ mV, $I_t = 60$ pA) of (b). (d) STM image ($V_s = -100$ mV, $I_t = 200$ pA) of the B-terminated surface. (e) Zoom-in STM image ($V_s = -100$ mV, $I_t = 60$ pA) of (d).

After low-temperature *in situ* cleavage of EuB_6, two stable surfaces are reproducibly observed in STM images. One surface shows a square atomic lattice and disordered corrugations (supplemental information Fig. 1(a)), and is assigned to the Eu-terminated surface. The relatively weak surface binding of Eu atoms can lead to aggregation or disorder after cleavage.[10] An ordered region of the Eu-terminated surface is shown in Fig. 1(b), where abundant defects are visible and appear as dark spots. The other surface is comparatively flat and is assigned to the B-terminated surface (Fig. 1(d)). Both terminated surfaces exhibit a regular square lattice (Fig. 1(c) and 1(e)) with a lattice constant of $\sim$ 4.14 Å, consistent with previous reports.[24] A high density of defects is observed on the B-terminated surface. Most defects show fourfold symmetry, while long-range lattice order remains preserved around them. The spectroscopic measurements and defect analyses discussed below focus on the B-terminated surface.

A wide-energy-range dI/dV spectrum is acquired from an intact lattice area of the B-terminated surface far from defects (Figs. 2(a) and 2(b)). The local density of states (LDOS) is higher in the valence band and exhibits a subtle kink near -0.4 V, while remaining very low above -0.2 V. By con-

trast, spectra taken on the Eu-terminated surface show the opposite trend, with a higher LDOS in the conduction band (supplemental information Figs. 1(b) and 1(c)), indicating that the two terminated surfaces contribute differently to the low-energy electronic structure. Consistent with previous studies, the valence-band states near the Fermi energy (E_F) mainly derive from B-2p orbitals, whereas the conduction-band states originate primarily from Eu-5d orbitals.[24,36,37]

Bias-dependent STM images of the B-terminated surface (supplemental information Figs. 2(a)–2(d)) further reveal that the spatial inhomogeneity around defects becomes more pronounced near −0.2 V and is relatively uniform at other biases. Previous angle-resolved photoemission spectroscopy (ARPES) studies reported that two low-energy subbands, α_2 (hole-like) and β_1 (electron-like), are nearly degenerate near −0.2 V.[37] A defect-induced local potential may therefore modify their relative spectral weight, leading to the observed bias-dependent contrast. Wide-energy-range $\mathrm{d}I/\mathrm{d}V$ spectra show no resolvable dependence on either in-plane or out-of-plane magnetic fields (supplemental information Figs. 3(a) and 3(b)).

To examine the low-energy excitations in more detail, $\mathrm{d}I/\mathrm{d}V$ spectra were acquired in a narrow energy window around E_F (Fig. 2(c)). The spectrum displays an approximately V-shaped background with multiple step-like features that appear nearly symmetrically about zero bias. A $\mathrm{d}I/\mathrm{d}V$ linecut taken along the dashed line in Fig. 2(a) shows that these kinks occur at nearly fixed energies over several nanometers, with only their intensities varying spatially (Figs. 2(d) and 2(e)). This behavior suggests the presence of a cascade of inelastic channels.

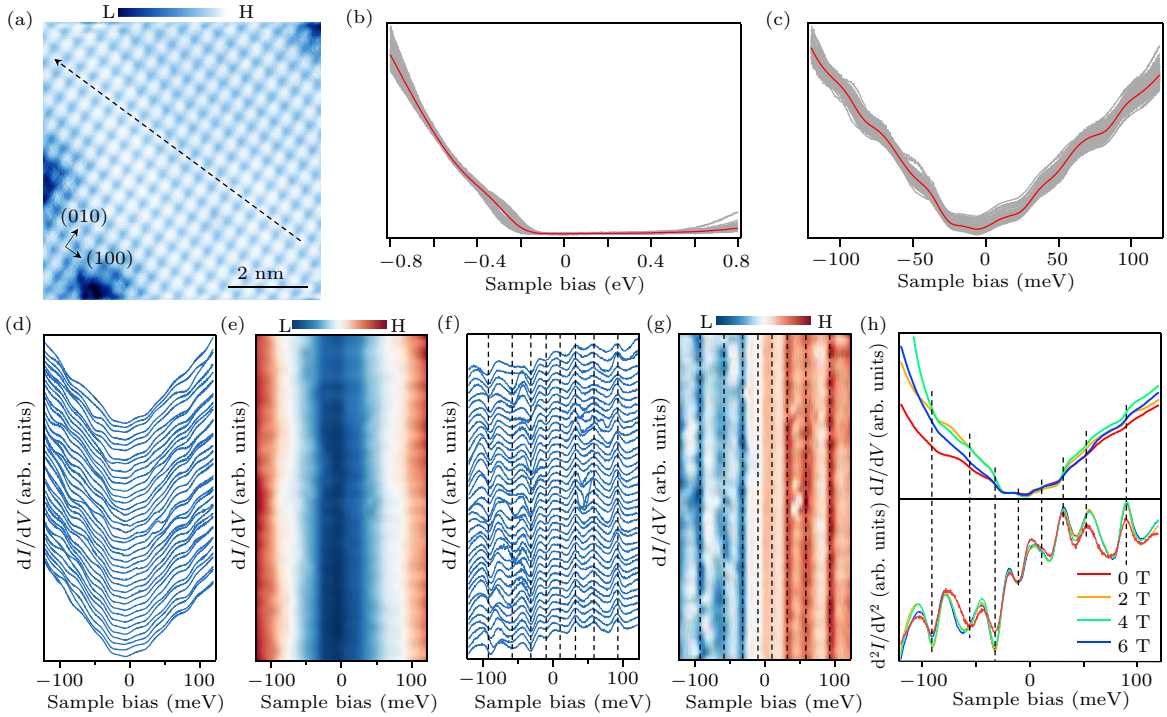


Fig. 2. Electronic properties and inelastic tunneling features on the B-terminated surface. (a) STM image ($V_s = -100$ V, $I_t = 600$ pA) of the B-terminated surface. (b) Averaged $\mathrm{d}I/\mathrm{d}V$ spectrum in a wide energy range. (c) Averaged $\mathrm{d}I/\mathrm{d}V$ spectrum in a narrow energy range around the Fermi level. (d), (e) $\mathrm{d}I/\mathrm{d}V$waterfall plot (d) and intensity map (e) of the linecut taken along the black dash line in (a). (f), (g) $\mathrm{d}^2I/\mathrm{d}V^2$ waterfall plot (f) and intensity map (g) of the linecut taken along the black dash line in (a). The dashed lines mark the energy positions of symmetric peak-dip pairs in IETS. (h) Top: comparison of $\mathrm{d}I/\mathrm{d}V$ spectra at zero field and under different applied magnetic fields; bottom: comparison of $\mathrm{d}^2I/\mathrm{d}V^2$ spectra at zero field and under magnetic fields of 2 T, 4 T, and 6 T. Dashed lines mark the energy positions of symmetric peak-dip pairs in IETS.

The corresponding $\mathrm{d}^2I/\mathrm{d}V^2$ spectrum at zero magnetic field (Fig. 2(h)) reveals a series of peak-dip structures characteristic of inelastic tunneling. The peak positions at positive bias are 11.4 ± 0.1 mV, 30.6 ± 0.1 mV, 55.0 ± 0.2 mV, and 92.1 ± 0.3 mV, with corresponding dips at negative bias, giving approximately symmetric features at -11.0 ± 0.3 mV, -31.2 ± 0.2 mV, -54.3 ± 0.2 mV, and -93.4 ± 0.6 mV. For consistency, the positive-bias peaks are used to define the energies of the inelastic channels. Each feature exhibits an asymmetric peak-dip line shape arising from interference between elastic and inelastic tunneling processes within the junction.[38]

Compared with reported Raman modes, the 93 meV mode matches the T_{2g} shear vibration of the B_6 octahedra.[7,32] The remaining lower-energy modes, however, lack one-to-one correspondence with previously reported Raman-active phonons. A spatially resolved $\mathrm{d}^2I/\mathrm{d}V^2$ linecut (Figs. 2(f) and 2(g)) confirms that the four inelastic channels remain at fixed energies while their intensities vary periodically in space. Furthermore, measurements performed under out-of-plane mag-

netic fields of $B_z = 2$ T, 4 T, and 6 T show no measurable shift in the inelastic channel energies (Fig. 2(h)). This field independence indicates that the observed inelastic channels originate from phonon excitations. It is worth noting that, as shown in the upper panel of Fig. 2(h), the $\mathrm{d}I/\mathrm{d}V$ background near E_F also changes under finite magnetic fields. This is consistent with the change in the LDOS induced by the spin-canting process and the ensuing topological phase transition as the magnetic field is increased along the [001] direction.[37] Therefore, the difference in IETS intensity between 0 T and finite fields more likely reflects the influence of the field-modulated low-energy electronic background on the spectral weight of the inelastic signals.

Atomic-resolution STM images reveal several representative defects on the B-terminated surface (Fig. 3(a)). Because the covalent B_6 octahedral network does not provide a natural cleavage plane, cleavage may occur either between neighboring octahedra, producing relatively regular surfaces, or by breaking B–B bonds within the octahedra, generating defects in the topmost or subsurface layers.[15,39] Based on their apparent symmetry and contrast in STM images, the observed defects can be classified into four types: type I (checkerboard; Fig. 3(b)), type II (X-shaped; Fig. 3(c)), type III (bright cross; Fig. 3(d)), and type IV (petal-like; Fig. 3(e)). Except for type I, the dominant elongation of type II–IV defects occurs along the (110) direction. This trend is likely associated with anisotropic relaxation or bond rearrangement in the surface or subsurface layers after B–B bond rupture in the B_6 octahedra. For type II–IV defects, the central B site (at the centers of the dashed orange squares in Figs. 3(c)–3(e)) appears markedly darker than the surrounding lattice, indicating that the defect strongly perturbs its nearest-neighbor atoms.[39]

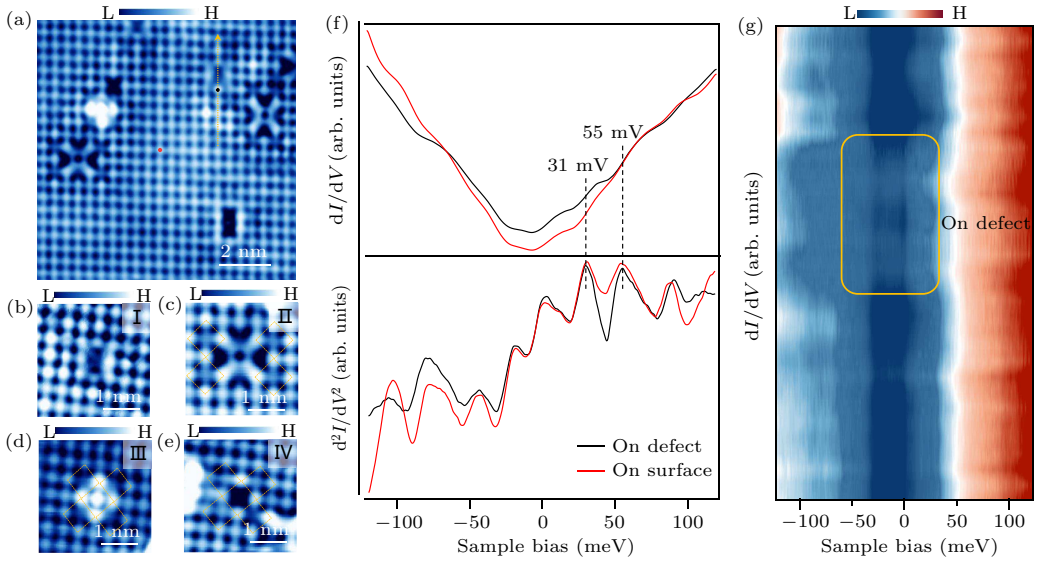


Fig. 3. Defect-induced modulation of low-energy electronic states and IETS. (a) STM image ($V_\mathrm{s} = -120$ mV, $I_\mathrm{t} = 1$ nA) of the B-terminated surface containing several defects. (b)–(f) Defects on the B-terminated surface ($V_\mathrm{s} = -100$ mV, $I_\mathrm{t} = 600$ pA) are classified according to their local appearance into four types: type I (checkerboard; (b)), type II (X-shaped; (c)), type III (bright cross; (d)), and type IV (petal-like; (e)). The central B sites within the orange dashed squares appear darker than the surrounding sites. (f) Comparison of $\mathrm{d}I/\mathrm{d}V$ (top) and $\mathrm{d}^2I/\mathrm{d}V^2$ (bottom) spectra acquired at the atom adjacent to a defect (black dot in (a)) and at a remote site in the intact lattice (red dot in (a)). Dashed lines mark the peak positions at 31 mV and 55 mV. (g) $\mathrm{d}I/\mathrm{d}V$ linecut intensity map taken along the orange dashed line across the defect in (a).

To examine their electronic influence, a representative type-I defect was selected for spectroscopic measurements. $\mathrm{d}I/\mathrm{d}V$ spectra acquired near the defect exhibit a shallower V-shaped profile compared with spectra obtained on intact lattice regions (Fig. 3(f)), indicating an enhancement of the LDOS, similar to behavior reported near defects in SmB_6.[39] A linecut across the defect further shows that the LDOS enhancement is largely confined to a single lattice site adjacent to the defect and decays rapidly with distance (Fig. 3(g)), indicating a short-range charge-density modulation on the lattice length scale. Bias-dependent $\mathrm{d}I/\mathrm{d}V$ maps obtained in regions containing multiple defect types reproducibly show similar local enhancement patterns (supplemental information Fig. 4), suggesting that this behavior is a general feature of the defect landscape rather than an isolated case. These observations indicate that disruption of B-2p dangling bonds and local reconstruction of the B_6 octahedra modify the local potential landscape and hybridization conditions of the surface states.[36] Despite these strong local electronic effects, the peak energies of the inelastic channels remain unchanged near defects, whereas the spectral intensities of the ~ 31 mV and ~ 55 mV phonon modes are suppressed. This indicates that defects primarily modulate the local electron–phonon coupling (EPC) strength rather than altering the phonon energies.

To further examine this effect, normalized IETS (N-IETS) maps, defined as $(\mathrm{d}^2I/\mathrm{d}V^2)/(\mathrm{d}I/\mathrm{d}V)$, are acquired in defect-rich regions at biases corresponding to the defect-sensitive phonon modes (Figs. 4(a)–4(c)). Compared with

conventional d^2I/dV^2, N-IETS suppresses variations arising from LDOS changes and more directly reflects the strength of electron–vibration coupling.[5,40–42] In the N-IETS maps at 33 mV and 55 mV, the inelastic signal is spatially inhomogeneous, indicating that the EPC strength is redistributed by the local environment. The signal is suppressed at defect centers and exhibits an anisotropic texture that follows the defect shape. One possible mechanism is that the local symmetry lowering introduced by the short-range modulation alters the selection rules and visibility of inelastic processes,[43] whereas local bond rearrangement near defects can renormalize vibrational states through changes in force constants.[32,44] Together, these effects can produce mode-selective enhancement of the EPC.

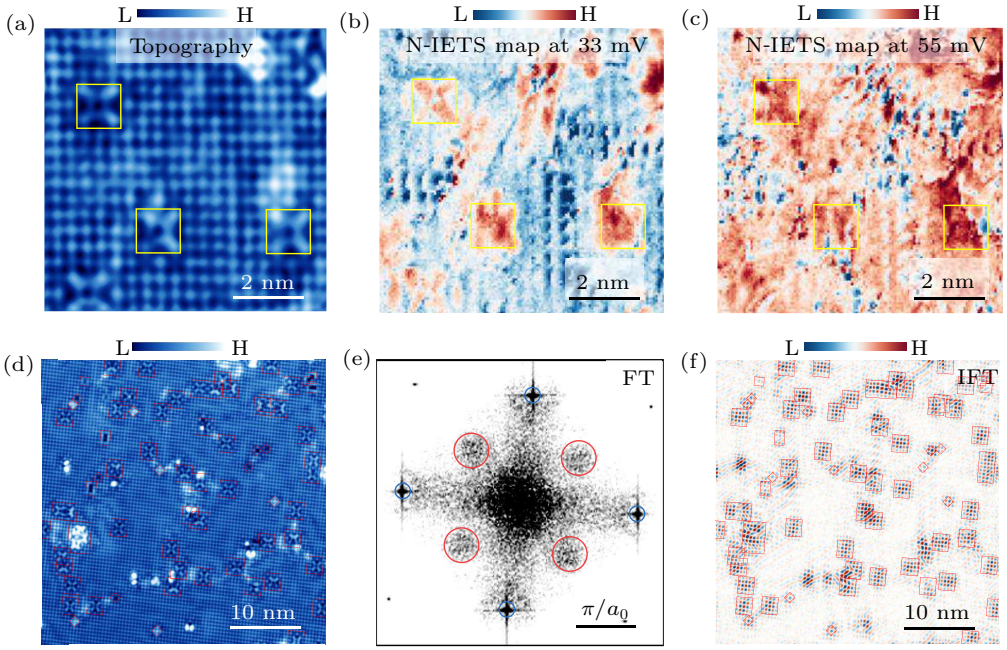


Fig. 4. Defect-pinned short-range $\sqrt{2}\times\sqrt{2}$ order and selective suppression of phonon modes. (a) STM topography ($V_s = -120$ mV, $I_t = 400$ pA) of the B-terminated surface with defects. (b), (c) Real-space normalized-IETS maps acquired at energies of 33 mV (b) and 55 mV (c), respectively. Yellow squares mark the defect sites and the associated short-range modulation. (d) Large-area STM image ($V_s = -120$ mV, $I_t = 400$ pA) of the B-terminated surface. (e) Two-dimensional Fourier transform of (d). Blue circles indicate the Bragg peaks of the B-terminated surface, and red circles highlight a pronounced diffuse enhancement near the M points of q-space, corresponding to a $\sqrt{2}\times\sqrt{2}$ short-range order. (f) Real-space map of the $\sqrt{2}\times\sqrt{2}$ order obtained by inverse Fourier transforming the red-circled region in (e). The red squares in (d) and (f) mark the defect sites and the associated short-range modulation, with a one-to-one correspondence between the two panels.

We next examine the influence of defects on the surrounding electronic structures. Large-area STM images of the B-terminated EuB_6 surface reveal a high density of defects (Fig. 4(d), red box). The corresponding Fourier transform image reveals, in addition to the Bragg peaks (Fig. 4(e), blue circles), a new order near the M points at $(\pm1/2, \pm1/2)$ (Fig. 4(e), red circles),[45] corresponding to a $\sqrt{2}\times\sqrt{2}$ $R45^\circ$ modulation. An inverse Fourier transform of this signal reveals that the $\sqrt{2}\times\sqrt{2}$ modulation is localized around individual defects and decays over $\sim$ 4–5 lattice constants (Fig. 4(f)). The $\sqrt{2}\times\sqrt{2}$ modulation can be reproducibly observed on the B-terminated surface of different EuB_6 samples and therefore shows a degree of universality. These observations indicate that the $\sqrt{2}\times\sqrt{2}$ short-range order is pinned by defects and produces a local lattice modulation that selectively modifies the near-neighbor LDOS and the local EPC strength. This defect-pinned lattice modulation naturally explains the spatial redistribution of the phonon-related inelastic signals.

In summary, IETS on the B-terminated surface of EuB_6 obtained by low-temperature cleavage resolves a cascade of stable inelastic channels at $\sim$ 11 mV, 31 mV, 55 mV, and 93 mV. Near defects, the LDOS around the E_F is elevated, whereas the energies of these inelastic channels remain nearly unchanged and their intensities are redistributed in a mode-selective manner. This behavior indicates that defects modulate the local phonon excitation probability and electron–phonon coupling strength. Furthermore, Fourier analysis of topography reveals a $\sqrt{2}\times\sqrt{2}$ short-range order in defect-proximal regions of the B-terminated surface. This defect-pinned lattice modulation selectively modifies the charge density and the local EPC strength on neighboring lattice sites. These results provide real-space insight into the interplay between surface phonons, defects, and low-energy electronic states in EuB_6.

Acknowledgements

The work is supported by the National Key Research and Development Program of China (Grant Nos. 2024YFA1207702 and 2022YFA1204100), the National

Natural Science Foundation of China (Grant No. 62488201), the CAS Project for Young Scientists in Basic Research (Grant No. YSBR-003), and the Quantum Science and Technology-National Science and Technology Major Project (Grant No. 2021ZD0302700).

References

[1] Cheong S W and Mostovoy M 2007 *Nat. Mater.* **6** 13
[2] Cui J, Boström E V, Ozerov M, Wu F, Jiang Q, Chu J H, Li C, Liu F, Xu X, Rubio A and Zhang Q 2023 *Nat. Commun.* **14** 3396
[3] Bao S, Gu Z L, Shangguan Y, Huang Z, Liao J, Zhao X, Zhang B, Dong Z Y, Wang W, Kajimoto R, Nakamura M, Fennell T, Yu S L, Li J X and Wen J 2023 *Nat. Commun.* **14** 6093
[4] Zhang X, Zhang Y, Okamoto S and Xiao D 2019 *Phys. Rev. Lett.* **123** 167202
[5] You S, Lü J T, Guo J and Jiang Y 2017 *Advances in Physics: X* **2** 907
[6] Calderón M, Wegener L and Littlewood P 2004 *Phys. Rev. B* **70** 092408
[7] Snow C, Cooper S, Young D, Fisk Z, Comment A and Ansermet J P 2001 *Phys. Rev. B* **64** 174412
[8] Nyhus P, Yoon S, Kauffman M, Cooper S, Fisk Z and Sarrao J 1997 *Phys. Rev. B* **56** 2717
[9] Süllow S, Prasad I, Bogdanovich S, Aronson M, Sarrao J and Fisk Z 2000 *J. Appl. Phys.* **87** 5591
[10] Wirth S and Schlottmann P 2021 *Adv. Quantum Technol.* **4** 2100102
[11] Gabani S, Flachbart K, Siemensmeyer K and Mori T 2020 *J. Alloy. Compd.* **821** 153201
[12] Hong J, Mutalik S, Pescarmona P P and Protesescu L 2024 *Chem. Mater.* **36** 2147
[13] Zabolotnyy V, Fürsich K, Green R, Lutz P, Treiber K, Min C H, Dukhnenko A, Shitsevalova N, Filipov V and Kang B 2018 *Phys. Rev. B* **97** 205416
[14] Coe A, Zhu Z H, He Y, Kim D J, Fisk Z, Hoffman J D and Hoffman J E 2025 *Phys. Rev. Lett.* **134** 236205
[15] Wirth S, Rößler S, Jiao L, Ale Crivillero M V, Rosa P F and Fisk Z 2021 *Phys. Status Solidi B* **258** 2000022
[16] Trenary M 2012 *Sci. Technol. Adv. Mater.* **13** 023002
[17] Degiorgi L, Felder E, Ott H, Sarrao J and Fisk Z 1997 *Phys. Rev. Lett.* **79** 5134
[18] Ogita N, Nagai S, Okamoto N, Udagawa M, Iga F, Sera M, Akimitsu J and Kunii S 2003 *Phys. Rev. B* **68** 224305
[19] Broderick S, Ruzicka B, Degiorgi L, Ott H R, Sarrao J L and Fisk Z 2002 *Phys. Rev. B* **65** 121102
[20] Zirngiebl E, Hillebrands B, Blumenröder S, Güntherodt G, Loewenhaupt M, Carpenter J M, Winzer K and Fisk Z 1984 *Phys. Rev. B* **30** 4052
[21] Basov D N, Averitt R D, Van Der Marel D, Dressel M and Haule K 2011 *Rev. Mod. Phys.* **83** 471
[22] Devereaux T P and Hackl R 2007 *Rev. Mod. Phys.* **79** 175
[23] Kim J H, Lee Y, Homes C, Rhyee J S, Cho B K, Oh S J and Choi E 2005 *Phys. Rev. B* **71** 075105
[24] Shen J, Gao J, Yi C, Li M, Zhang S, Yang J, Wang B, Zhou M, Huang R and Wei H 2023 *Innovation* **4** 100399
[25] Fisk Z, Johnston D, Cornut B, Von Molnar S, Oseroff S and Calvo R 1979 *J. Appl. Phys.* **50** 1911
[26] Kim J, Kim Y J, Kuneš J, Cho B K and Choi E 2008 *Phys. Rev. B* **78** 165120
[27] Kim J, Ku W, Lee C C, Ellis D, Cho B, Said A, Shvyd'ko Y and Kim Y J 2013 *Phys. Rev. B* **87** 155104
[28] Pan L, Wang Y, Ding X, Hu G, Guo H, Lv S, Xian G, Qi Q, Zhu K, Han Y, Lei M, Li Z, Bao L, Zhang Y, Lin X, Zhu S, Peng R, Yang H and Gao H J 2024 *Appl. Phys. Lett.* **125** 243101
[29] Zhu K, Qi Q, Xie Y, Pan L, Lv S, Hu G, Zhao Z, Xian G, Han Y, Bao L, Zhang Y, Lin X, Guo H, Yang H and Gao H J 2025 *Chin. Phys. B* **34** 097308
[30] Süllow S, Prasad I, Aronson M, Sarrao J, Fisk Z, Hristova D, Lacerda A, Hundley M, Vigliante A and Gibbs D 1998 *Phys. Rev. B* **57** 5860
[31] Manna R S, Das P, de Souza M, Schnelle F, Lang M, Müller J, von Molnár S and Fisk Z 2014 *Phys. Rev. Lett.* **113** 067202
[32] Martinho H, Rettori C, Dalpian G, Da Silva J, Fisk Z and Oseroff S 2009 *J. Phys.: Condens. Matter* **21** 456007
[33] Noguera C 2000 *J. Phys.: Condens. Matter* **12** R367
[34] Buchsteiner P, Harmsen L, Ciomaga Hatnean M, Balakrishnan G and Wenderoth M 2020 *Phys. Rev. B* **102** 205403
[35] Wu Z B, Gao Z Y, Chen X Y, Xing Y Q, Yang H, Li G, Ma R, Wang A, Yan J and Shen C 2018 *Rev. Sci. Instrum.* **89** 113705
[36] Rößler S, Jiao L, Seiro S, Rosa P F, Fisk Z, Rößler U K and Wirth S 2020 *Phys. Rev. B* **101** 235421
[37] Gao S Y, Xu S, Li H, Yi C J, Nie S M, Rao Z C, Wang H, Hu Q X, Chen X Z and Fan W H 2021 *Phys. Rev. X* **11** 021016
[38] Lambe J and Jaklevic R 1968 *Phys. Rev.* **165** 821
[39] Ruan W, Ye C, Guo M, Chen F, Chen X, Zhang G M and Wang Y 2014 *Phys. Rev. Lett.* **112** 136401
[40] De La Torre B, Švec M, Foti G, Krejčí O, Hapala P, Garcia-Lekue A, Frederiksen T, Zbořil R, Arnau A and Vázquez H 2017 *Phys. Rev. Lett.* **119** 166001
[41] Kim Y, Hellmuth T J, Burkle M, Pauly F and Scheer E 2011 *ACS nano* **5** 4104
[42] Okabayashi N, Paulsson M, Ueba H, Konda Y and Komeda T 2010 *Phys. Rev. Lett.* **104** 077801
[43] Lorente N, Persson M, Lauhon L J and Ho W 2001 *Phys. Rev. Lett.* **86** 2593
[44] Nguyen T H, Nguyen T M H, Kang B, Cho B, Han M, Choi H J, Kong M, Lee Y and Yang I S 2019 *J. Raman. Spectrosc.* **50** 1661
[45] Buchsteiner P, Sohn F, Horstmann J, Voigt J, Ciomaga Hatnean M, Balakrishnan G, Ropers C, Blöchl P and Wenderoth M 2019 *Phys. Rev. B* **100** 205407